Journal of Colloid and Interface Science 623 (2022) 947–961

Contents lists available at ScienceDirect

Journal of Colloid and Interface Science

journal homepage: www.elsevier.com/locate/jcis

Rational design of MXene/activated carbon/polyoxometalate triple hybrid electrodes with enhanced capacitance for organic-electrolyte supercapacitors

Jun-Jie Zhu [a,*], Avireddy Hemesh [b], Jordi Jacas Biendicho [b], Luis Martinez-Soria [a], Daniel Rueda-Garcia [a], Joan Ramon Morante [b,c], Belen Ballesteros [a], Pedro Gomez-Romero [a,d,*]

[a] Catalan Institute of Nanoscience and Nanotechnology (ICN2), CSIC and BIST, Campus UAB, Bellaterra, 08193 Barcelona, Spain
[b] Catalonia Institute for Energy Research (IREC), Jardins de les Dones de Negre 1, 08930, Sant Adrià de Besòs, Spain
[c] Faculty of Physics, University of Barcelona, Barcelona, Spain
[d] Consejo Superior de Investigaciones Científicas (CSIC), Spain

HIGHLIGHTS

- POMs were nano-dispersed within MXene with assistance of AC matrix.
- The hybrid combined the merits and compensate for the demerits of each component.
- Gravimetric capacitance of the hybrid was 2.2 times that of MXene.
- POMs remained anchored in the long-term leading to great cycle stability.
- Hybrid's asymmetric cells outperformed AC//MXene cells by weight and volume.

GRAPHICAL ABSTRACT

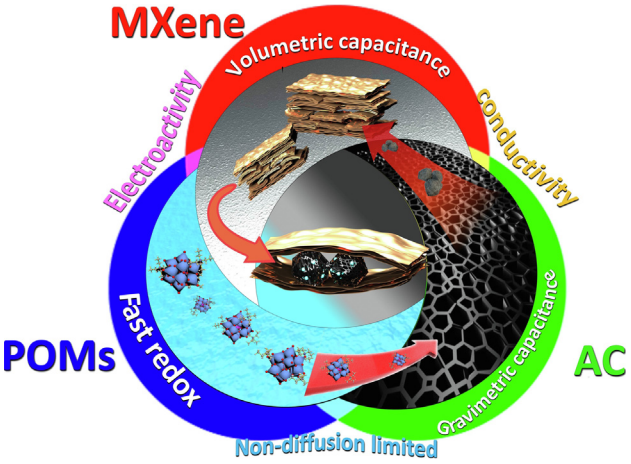

ARTICLE INFO

Article history:
Received 13 January 2022
Revised 26 April 2022
Accepted 28 April 2022
Available online 5 May 2022

Keywords:
Hybrid electroactive materials
MXene
Polyoxometalates
Organic
Supercapacitors

ABSTRACT

We report a triple hybrid electrode (MXene/activated carbon (AC)/polyoxometalates (POMs)) combining the merits of three materials: MXene (high volumetric capacitance), AC (high gravimetric capacitance) and Phosphotungstate (fast redox). Phosphotungstic acid (HPW12) and tetraethylammonium phosphotungstate (TEAPW12) were the two POMs used to prepare MXene/AC/POMs triple hybrids. MXene/AC/TEAPW12 outperformed MXene/AC/HPW12 in 1 M tetraethylammonium tetrafluoroborate (TEABF4)/acetonitrile. Nano-dispersion of POMs facilitates charge storage through surface capacitive processes (91% at 2 mV s^{-1}). MXene/AC/TEAPW12 delivered significantly higher gravimetric capacitance (87F g^{-1} at 1 mV s^{-1}) than MXene (40F g^{-1} at 1 mV s^{-1}) in the same organic electrolyte, without sacrificing much volumetric capacitance (less than 10%). The gravimetric capacitance of the triple hybrid was similar to that of MXene/AC, whereas its volumetric capacitance was 1.5 times higher. Replacing TEA cations with 1-ethyl-3-methylimidazolium cations ($EMIM^+$), the capacitance improved by 21%. Coupled with AC positive electrodes in an asymmetric cell, MXene/AC/TEAPW12 delivered 4.6 times higher gravimetric energy density and 3.5 times higher volumetric energy density than a similar MXene asymmetric cell

* Corresponding authors at: ICN2, Campus UAB, 08193 Bellaterra (Barcelona), Spain.
E-mail addresses: zhu.junjie@icn2.cat (J.-J. Zhu), pedro.gomez@icn2.cat (P. Gomez-Romero).

https://doi.org/10.1016/j.jcis.2022.04.170

at relatively high-power densities. This study proves that MXene/AC/TEAPW12 combines the merits and compensates for the demerits of each component and is a promising electrode material for organic-electrolyte supercapacitors.

1. Introduction

Energy storage devices with high energy density, power density and long lifespan are in urgent demand for a growing number of applications. Supercapacitors are a good starting point for this challenge since they feature intrinsically high power density and long cycle life. However, they run short of energy density. There are two main ways to increase the energy density of supercapacitors: i) increasing working voltage through the use of organic electrolytes, and ii) increasing storage capacity by a proper choice of electrode materials or through hybridization[1]. In this study, we followed both approaches based on the design of complex but unique hybrid materials leading to an optimal combination of charge storage capacity and high conductivity together with the high voltage range typical of organic electrolytes.

We first needed a material with a very high volumetric capacitance, and MXenes excel in this respect as they constitute a family of two-dimensional materials, usually containing one layer of transition metal and one layer of carbide. MXenes have a general formula $M_{n+1}X_nT_x$, where M is a transition metal, X is carbon and/or nitrogen, n is an integer between 1 and 3, and T_x represents surface functional groups[2]. A conductive inner transition metal carbide layer enables fast electron supply to electrochemically active sites, which makes of MXenes promising electrode materials for supercapacitors[3].

MXenes stand out from their competitors because of the high volumetric capacitance[4–6], the key parameter for the industry when compactness is required. In this scenario, titanium carbides ($Ti_3C_2T_x$) is the most widely studied and developed MXene, which has been found to deliver a volumetric capacitance as high as 900F cm^{-3} in an aqueous electrolyte[3].

Conventional aqueous electrolytes allow for a stable potential window of less than 1.5 V. Since energy density is proportional to the square of the voltage, other electrolytes like "water-in-salt" electrolytes (with V = 2.2 V)[7], organic electrolytes (with V = 2.7 V)[8] or ionic liquids (with V > 3 V)[9,10] have been preferred for a rational optimized design. Indeed, several groups have already attempted to use MXene in organic electrolytes. Some examples include MXenes for lithium-ion capacitors [11,12], sodium-ion capacitors [13], or just supercapacitors with conventional organic electrolytes[8,13–15]. Some experimental drawbacks have already been described in these types of applications. For example, contrary to the previous hypothesis, $Ti_3C_2T_x$ MXene provides much lower specific capacitance in conventional organic electrolytes (less than 40 F g^{-1} or 70 F cm^{-3} in 1 M TEABF4 in acetonitrile[16]) than in aqueous electrolytes. Various approaches have been followed to enhance the energy storage capabilities of MXenes, including expanding interlayer distance by other nanomaterials or functional groups[5,17–22], increasing active sites by making porous MXenes[23,24], or trying to introduce active materials[25–31], including polyoxometalates (POMs)[19,32]. However, these attempts have failed to intercalate POMs into MXenes and have led to mixed phases instead[32].

POMs constitute a family of nanometric metal oxide clusters, able to provide fast reversible multi-electron redox reactions not limited by diffusion[33–35]. As such, POMs have been used as active materials, just by themselves[35,36] or as active components in hybrid materials[33,35,37–41] in many kinds of energy storage devices. In these devices, their proper dispersion at the nanoscale and long-term anchoring onto a conducting substrate are key issues for fully harnessing the fast reversible multi-electron redox activity characteristic of POMs. Several porous materials, such as activated carbon[39,41,42], and 2D materials, for example, reduced graphene oxide (rGO)[38,40], have been shown to effectively anchor POMs[39,40]. The resulting hybrid materials have shown enhanced performance, including capacitance[38–42], and even increased potential window[39].

The synthesis of hybrid materials made of MXenes and POMs has been tackled by various authors. For example, Chen et al.[25] modified $Ti_3C_2T_x$ MXene with Keggin-type POMs by ionic liquid polymer linker but used it in low voltage aqueous electrolytes. Chao et al.[32] proposed the in-situ growth of Keplerate-type POMs on $Ti_3C_2T_x$ MXene, leading to a hybrid material with interesting performance in lithium-ion capacitors and sodium-ion capacitors. However, in their study, the first report needed the use of a linker to bond the acid form of a POM to MXene and its use was restricted to aqueous electrolytes. And while the second used organic electrolytes they failed to disperse POMs, leading to a material made of a mixture of phases, namely, MXene and crystallized POM. Thus, in both cases there was a failure to harness the full potential of POMs combined with MXene while working in a high-voltage organic electrolyte.

Accordingly, this was our goal, and in order to achieve it, we made use of activated carbon (AC) as a "transporting" phase for POMs, since, in a previous study, we had shown that this dual hybrid material can work in organic solvents, with properly dispersed POMs with their electroactivity not limited by diffusion [33].

Our working hypothesis was supported by our earlier work on AC/POM hybrids, which showed proper dispersion of POM clusters through physical adsorption in micropores, leading to materials able to operate both in aqueous or organic electrolytes[39,42,43]. Likewise, "hybrid" MXene/AC flexible electrodes have also been reported, with activated carbon facilitating the charge transfer from the electrode[16].

With these considerations in mind, we decided that a triple hybrid material formed by MXene, AC and POM could provide a complex but versatile system, in a rational design to produce a multifunctional electrode for energy storage[44]. Herein, we report the results of our work, which demonstrate that the MXene/AC/POM system can be made to optimize the functionality of each of the three components, leading to enhanced volumetric and gravimetric capacitances in an organic electrolyte symmetric supercapacitor.

2. Experimental

2.1. Synthesis of MXene ($Ti_3C_2T_x$)

MXene ($Ti_3C_2T_x$) was synthesized through a LiF/HCl etching method[45]. Namely, 0.5 g MAX phase (Ti_3AlC_2, 99%, Y-Carbon ltd.) was added slowly into a mixture of 0.5 g LiF (>99.99%, Sigma-Aldrich) and 10 mL 9 M HCl solution (diluted from 37% HCl, Sigma-Aldrich). The etching process was carried out in a capped Teflon-vessel for 24 h at 35°C. For washing and delamination, the mixture was poured into a 50 mL centrifugation tube and

washed with deionized water by centrifugation at 3500 rpm for 5 min. The supernatant was discarded. This step was repeated for several cycles until the pH of the dark-green supernatant was > 6. The sediments at the bottom expanded upon washing, which indicated delamination. Finally, the sediments were dispersed in water by hand-shaking and deaerated with Ar for 20 min and stored in the fridge for future use. A certain amount of the MXene colloid was filtered-off on a Celgard 3501 membrane to determine the concentration and for further use. The as-prepared electrode had a thickness of 11 ± 1 μm and an areal density of 3 ± 0.3 mg·cm^{-2}.

2.2. Synthesis of MXene/HPW12

20 mL MXene colloid (around 1 mg mL^{-1}) was mixed with 20 mL 10 mM phosphotungstic acid ($H_3PW_{12}O_{40}$(HPW12), reagent grade, Sigma-Aldrich) solution, and probe-sonicated for 1 h under circulating cooling water at 10 °C. The mixture was filtered-off and washed with Milli-Q water until the filtrate was neutral. The product was peeled off from the membrane, dried in a vacuum oven at 60 °C and stored in an argon-filled glovebox. The as-prepared sample (MXene/HPW12) could serve as a free-standing electrode. The as-prepared electrode had a thickness of 13 ± 1 μm and an areal density of 3.3 ± 0.3 mg cm^{-2}.

2.3. Synthesis of MXene/AC/HPW12

0.05 g activated carbon (DLC Super 30 from Norit Chemical) and 1.44 g phosphotungstic acid (HPW12) were added into 50 mL MXene colloid (around 1 mg mL^{-1}) and kept in probe-sonication for 1 h under circulating cooling water to keep the temperature below 10 °C. Subsequently, the mixture was filtered-off onto a Celgard 3501 membrane to get a free-standing electrode. The as-prepared electrode had a thickness of 24 ± 2 μm and an areal density of 2.8 ± 0.2 mg cm^{-2}.

2.4. Synthesis of MXene/AC/TEAPW12

AC/TEAPW12 was prepared following our previously reported method[33]. Then, 0.05 g AC/TEAPW12 was added into 50 mL MXene colloid (around 1 mg mL^{-1}) and kept in probe-sonication for 1 h under circulating cooling water to keep the temperature below 10 °C. The mixture was filtered-off onto Celgard 3501 membrane to obtain a free-standing electrode. The as-prepared electrode had a thickness of 21 ± 2 μm and an areal density of 2.4 ± 0.2 mg cm^{-2}.

For comparison, MXene/TEAPW12 and MXene/AC were also prepared and characterized (Figs. S1, S2 and S10).

2.5. Material characterization

Powder X-ray diffraction (XRD) patterns were collected on a PANalytical X'pert Pro-MRD diffractometer with Cu K_α radiation(λ = 1.5406 Å) and PIXel detector. The interlayer distance (d) of the (002) planes was determined by Bragg's law:

$$d = \frac{\lambda}{2sin\theta} \quad (1)$$

where λ is the X-ray wavelength,θ is the the diffraction angle.

Scanning electron microscopy (SEM) images were taken on a Quante 650 FEG microscope. For energy-dispersion X-ray spectra (EDX) semi-quantitative analysis, we averaged the elemental analysis of five spectra to present the final results. High resolution transmission electron microscopy (HR-TEM) images, high angle annular dark field scanning transmission electron microscopy (HAADF-STEM) images, and selected area electron diffraction (SAED) patterns were obtained from an FEI Tecnai G2 F20 microscope. Volumetric N_2 sorption isotherms were collected at 77 K (N_2) using an ASAP 2020 HD (Micromeritics). Pore size distribution was estimated using a density functional theory (DFT) model (N_2-cylindrical pores-oxide surface) implemented in the Microactive 4.00 software with a regularization factor of 0.01. X-ray photoelectron spectra were collected on Phoibos 150 probe from SPECS. Peak fitting for the high-resolution spectra was performed using CasaXPS Version 2.3.1. Before the peak fitting, the background was subtracted using a Shirley function.

2.6. Electrochemical characterization

T-type Swagelok cells were applied to fabricate three-electrode configuration. The working electrodes were cut into 10 mm round pieces and the overloaded activated carbon counter electrodes were cut into 12 mm round pieces. 0.01 M Ag/Ag$^+$ served as the reference electrode. 1 M TEABF4 in acetonitrile or 1 M EMIMTFSI in acetonitrile served as the electrolyte. CR2032 coin cells were used to fabricate asymmetric devices. The electrochemical tests were carried out in an Argon-filled glove box with the oxygen and water lever under 5 ppm.

The gravimetric capacitance (C_m) and the volumetric capacitance (C_v) were calculated from cyclic voltammograms (CVs) according to the following equations:

$$C = \frac{\int I(V) \cdot dV}{2v\Delta V} \quad (2)$$

$$C_v = \frac{C}{V_e} \quad (3)$$

$$C_m = \frac{C}{m} \quad (4)$$

where $\int I(V) \cdot dV$ is the integral area of CVs, v is the scan rate, ΔV is voltage window, V_e is the volume (cm^3) of the electrode and m is the mass (g) of the electrode.

The gravimetric energy density E_m (Wh kg^{-1}) and volumetric E_v energy density E_v (Wh cm^{-3}), gravimetric power density P_m(W kg^{-1}) and volumetric power density P_v (W cm^{-3}) were calculated from the two-electrode cell discharge data using the following equations:

$$E_m = \frac{C\Delta V^2}{3.6 \times 2m_{total}} \quad (5)$$

$$E_v = \frac{C\Delta V^2}{3600 \times 2V_{total}} \quad (6)$$

$$P_m = \frac{1000 \times I\Delta V}{m_{total}} \quad (7)$$

$$P_v = \frac{I\Delta V}{V_{total}} \quad (8)$$

where m_{total} is the total mass (g) of the two electrodes, V_{total} is the total volume (cm^{-3}) of the two electrodes, and I is the discharging current (A).

3. Results and discussion

The crystal structure of the solid phases was characterized by XRD. Fig. 1 presents the XRD patterns of the pristine MXene and derived materials. Table 1 shows the positions of (002) diffraction peaks and the interlayer distance. All the XRD patterns confirm the

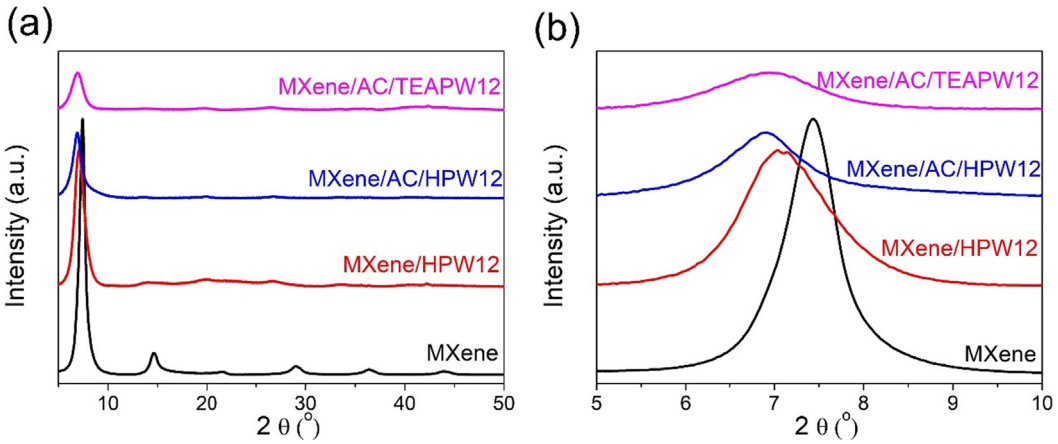

Fig. 1. (a) XRD patterns of pristine MXene, MXene/HPW12, MXene/AC/TEAPW12 and MXene/AC/HPW12. (b) Zoom-ins of (a) in the 5–10° 2θ range showing (002) peaks.

layered structure of the pristine MXene and the hybrid materials but with different interlayer distances and various crystallinity.

As can be observed, the pristine MXene has its (002) peak centred at 7.44°, and an interlayer distance of 11.87 Å, which is in the typical range of LiF/HCl-etched $Ti_3C_2T_x$ MXene[45]. The (002) peak of MXene/HPW12 is broader, revealing a poorer crystallinity, probably associated with the powerful probe-sonication that broke down large nanosheets. In this case, the peak shifts towards smaller two theta angles. On the other hand, the interlayer distance of 12.42 Å, is only slightly larger than that of the pristine MXene. Arup Chakraborty et al. have recently pointed out that even small anions such as Cl^- and Br^- are difficult to insert into MXenes[46]. Since PW12 anions are 1 nm in diameter, significantly larger than pre-intercalated Li^+, we conclude that the PW12 clusters are not intercalated into MXene but are mainly anchored on the surface. The XRD pattern of MXene/AC/HPW12 presents a broad peak at around 6.91°, corresponding to a slightly larger interlayer distance (12.80 Å) compared with MXene. The AC particles are micron scale. Thus, neither AC nor PW12 clusters can insert MXene layers. The slight variation of interlayer distance is supposed to be associated with the fact that high-power sonication slightly increases interlayer distance[47]. Furthermore, the sonication during the preparation and the amorphous AC reduced the overall crystallinity of the final material. For the same reasons, the XRD pattern of MXene/AC/TEAPW12 presents a similarly broad peak, with minor shifting with respect to the pristine MXene. The XRD patterns of the hybrid materials (MXene/HPW12, MXene/AC/HPW12 and MXene/AC/TEAPW12) do not exhibit any other peaks corresponding to HPW12 nor TEAPW12. This is very significant since it rules out the inclusion of the POMs as crystallized extended phases. Instead, XRD results are consistent either with the absence of POMs in the hybrid or with POM clusters being dispersed individually or at most in groups small enough to prevent bulk diffraction. The following EDX analyses in Table 2, confirm the existence of tungsten (PW12).

In order to observe the morphology and evaluate the loading mass of PW12 clusters, the samples were characterized under the scanning electron microscope equipped with energy-dispersive X-ray spectroscopy. The pristine MXene (Fig. 2a) exhibits an accordion-like structure, which remains even after suffering high-power probe-sonication (MXene/HPW12, Fig. 2b). For the MXene/HPW12 material, we cannot detect or discern any other heterogeneous aggregates, but the EDX spectrum confirms the presence of PW12 clusters, not apparent most likely due to the small nanosize of the PW12 clusters (1 nm). MXene/AC/HPW12 (Fig. 2c) and MXene/AC/TEAPW12 (Fig. 2d) exhibit a similar morphology, different from pristine MXene with the particles spreading on or surrounded by nanosheets. Since in the XRD patterns of MXene/AC/HPW12 and MXene/AC/TEAPW12 we cannot discern any diffraction peaks except those from MXene, we confirmed that the particles were amorphous AC, with dispersed, not well-crystallized PW12 clusters. We have previously shown that AC is an ideal matrix for absorbing PW12 and spreading them in nanopores[39]. We therefore propose that most PW12 clusters are absorbed on AC in these triple hybrid materials, as proven in the EDX spectra and HAADF-STEM images, shown in the following Table 2 and Fig. 4.

Table 2 lists the weight percentage of tungsten and titanium derived from EDX spectra. MXene/HPW12 only contains 6 wt% tungsten even with the assistance of high-power sonication, revealing that MXene is not a good substrate for direct-anchoring of POMs. That is most likely the reason why most previous studies had to resort to linking groups[48,49] or in-situ synthesis[32]. Indeed, through the in-situ synthesis (synthesis of MXene/TEAPW12, in supplementary materials), we could load a large amount of TEAPW12 on MXene (Table S1). As for MXene/AC/HPW12, improvement in the loading mass of PW12 must be ascribed to the inclusion of AC in the material providing a microporous matrix for anchoring POMs. MXene/AC/TEAPW12 contains less W than Mxene/AC/HPW12 because we carried out an ex-situ synthesis, in which TEAPW12 clusters had been already immobilized in AC accounting for 37.5 wt% in AC/TEAPW12 precursor.

Table 1
The positions of (002) peaks and their corresponding interlayer space derived from the XRD patterns.

Sample	2θ values for (002) diffraction peaks/°	Interlayer distance/Å
MXene	7.44	11.87
MXene/HPW12	7.09	12.42
MXene/AC/TEAPW12	6.91	12.80
MXene/AC/HPW12	6.95	12.71

Table 2
Semi-quantitative analysis result from EDX spectra.

Sample	Ti/ wt. %	W/ wt. %
Mxene/HPW12	51.2 ± 3.6	6.1 ± 1.1
Mxene/AC/HPW12	31.4 ± 2.1	17.5 ± 2.0
Mxene/AC/TEAPW12	39.7 ± 2.8	13.5 ± 1.8

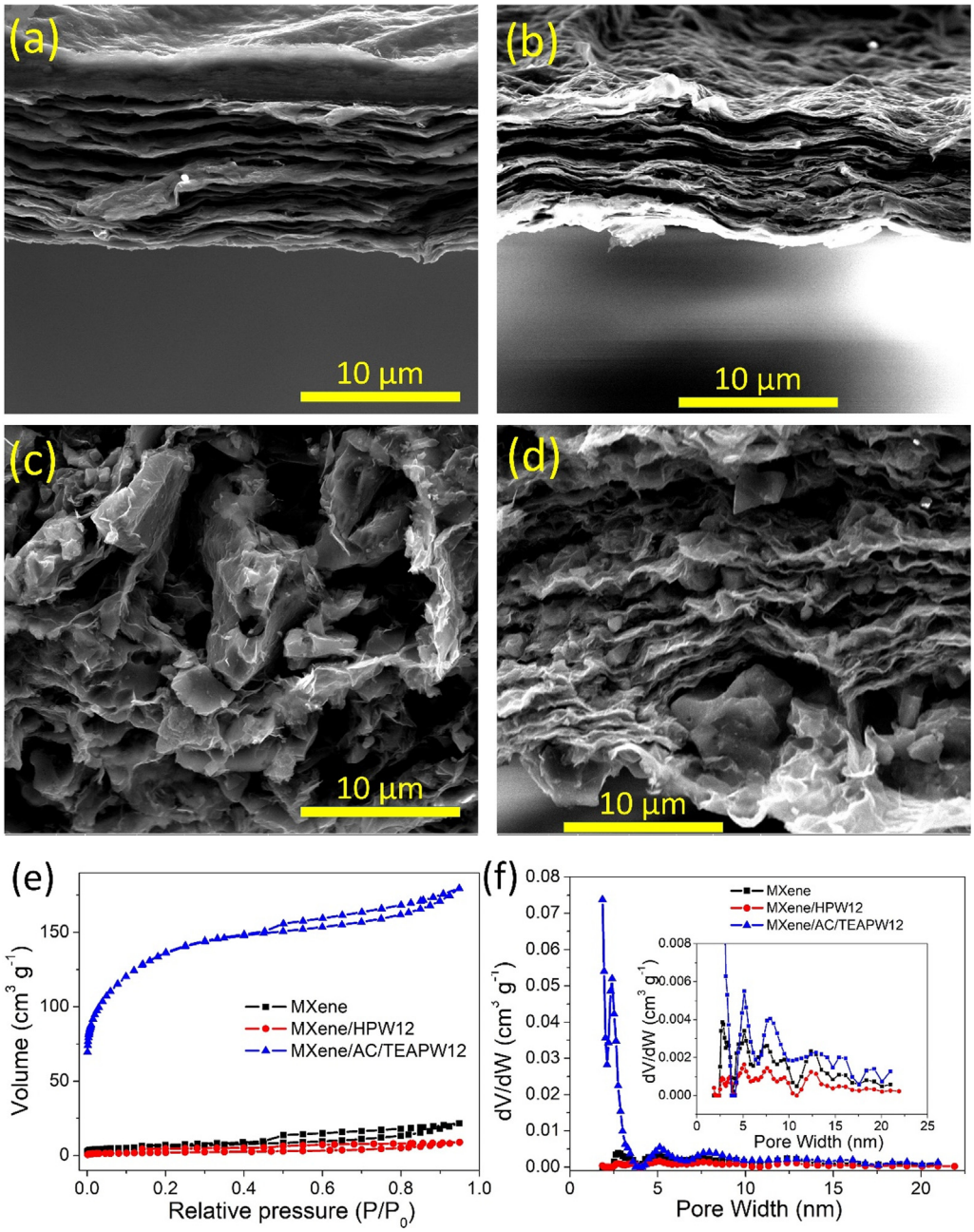

Fig. 2. SEM images of (a) MXene, (b) MXene/HPW12, (c) MXene/AC/HPW12 and (d) MXene/AC/TEAPW12. (e) N_2 sorption isotherms and (f) pore size distribution curves of MXene, MXene/HPW12 and MXene/AC/TEAPW12.

Since the SEM images reveal a remarkable expansion of the space among MXene nanosheets due to the AC particles, we carried out volumetric N_2 sorption experiments to investigate the influence of the inclusion of HPW12 or AC/TEAPW12 on the porous properties of MXene. Fig. 2e presents the nitrogen sorption isotherms of MXene, MXene/HPW12 and MXene/AC/TEAPW12. MXene/AC/TEAPW12 exhibits a significantly larger absorbed volume. The specific surface area of MXene/AC/TEAPW12 is 499 m^2 g^{-1}, 30 times larger than pristine MXene (15 m^2 g^{-1}), which we ascribe to the microporous nature of AC/TEAPW12 (specific surface area = 1007 m^2 g^{-1})[33]. The pore-size distribution (Fig. 2f) reveals that MXene/AC/TEAPW12 exhibits a hierarchical porous structure characterized by the dominance of AC micropores and the development of the mesopores inherited from MXene. While the inclusion of AC/TEAPW12 promotes mesopore formation, the addition of HPW12 leads to a decrease of specific surface area (from 15 m^2 g^{-1} to 7.8 m^2 g^{-1}), the pore structure remains the same (Fig. 2f). This can be explained by the heavy molecular weight of HPW12 as well as the fact that HPW12 clusters occupy some mesopores.

In order to compare the surface composition, bonding forming and element valence, we carried out XPS analysis on the pristine MXene, the double hybrid (MXene/HPW12) and the triple hybrid material (MXene/AC/TEAPW12). The low-resolution survey spectra (Fig. 3a) show that in addition to elements Ti, C, F, Cl and O that compose MXene, the hybrid materials (MXene/HPW12 and MXene/AC/TEAPW12) contain element W (Fig. 3a inset, W 4d peaks). The elemental compositions calculated by XPS are presented in Table S2, which shows that MXene/AC/TEAPW12 has a higher W atomic ratio than MXene/HPW12.

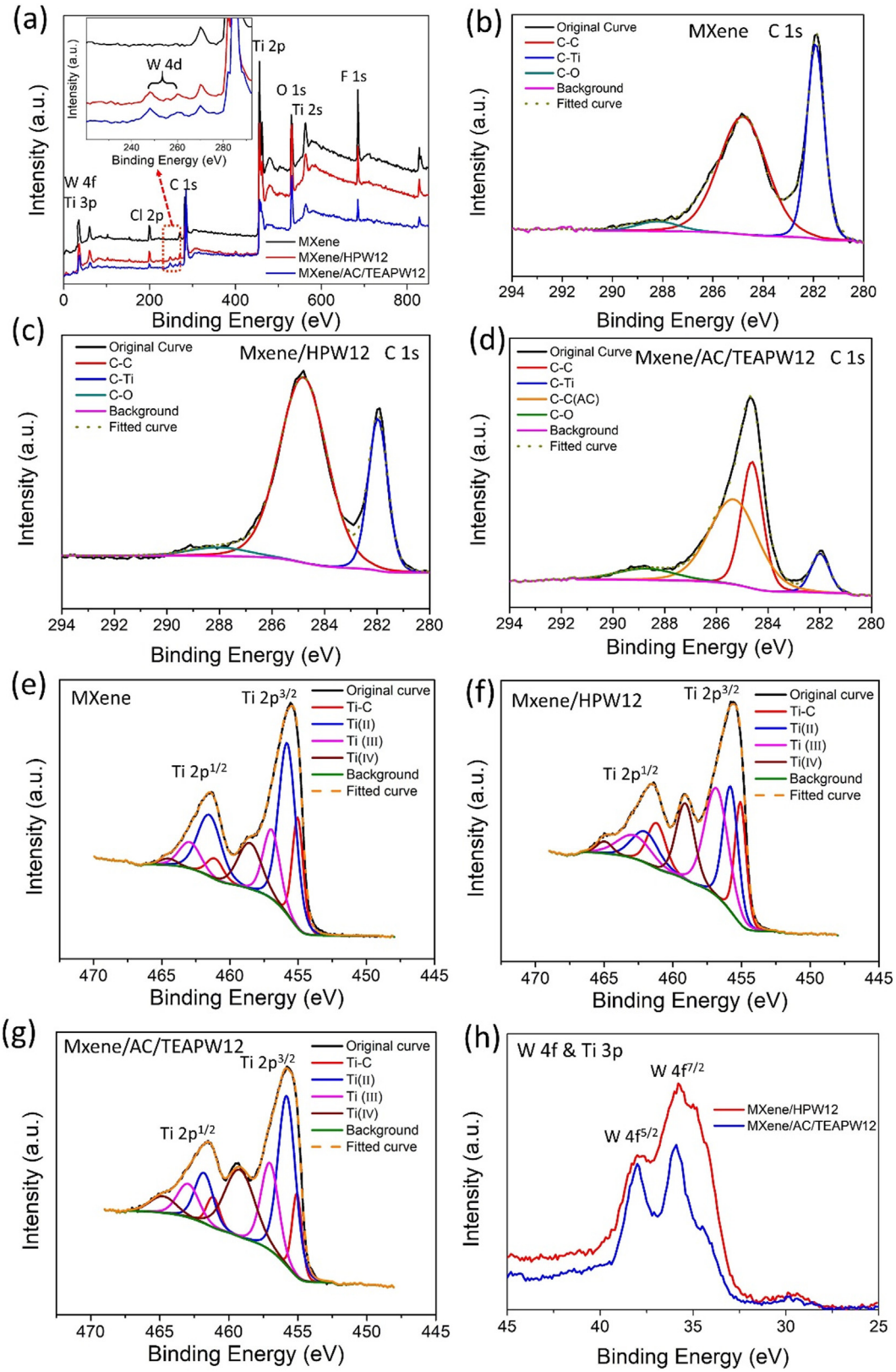

Fig. 3. (a) XPS full spectrum of MXene, MXene/HPW12 and MXene/AC/TEAPW12 (inset is the zoom-in area to discern W 4d peaks). C 1 s spectra of (b) MXene, (c) MXene/HPW12 and (d) MXene/AC/TEAPW12. Ti 2p spectra of (e) MXene, (f) MXene/HPW12 and (g) MXene/AC/TEAPW12. (g) W 4f spectra of MXene/HPW12 and MXene/AC/TEAPW12 (Ti 3p overlap).

Fig. 3b-d illustrate the C 1 s spectra of MXene, MXene/HPW12 and MXene/AC/TEAPW12. The pristine MXene and MXene/HPW12 show three peaks located at 281.85, 284.8 and 288.1 eV, which are matched to C–Ti, C—C and C—O, respectively. The MXene/AC/TEAPW12 shows an extra peak at 285.3 eV, which we attribute to the C—C bonds in AC. Fig. 3e-g depict the Ti 2p spectra of MXene, MXene/HPW12 and MXene/AC/TEAPW12, in which the Ti–C ($2p^{3/2}$ 455.0 eV, $2p^{1/2}$ 461.1 eV), Ti(II) ($2p^{3/2}$ 455.8 eV, $2p^{1/2}$ 461.5 eV), Ti(III) ($2p^{3/2}$ 457.0 eV, $2p^{1/2}$ 462.9 eV) and Ti(IV)($2p^{3/2}$ 458.6 eV, $2p^{1/2}$ 464.4 eV) peaks agree well with results from previous research[50,51]. Ti(II) and Ti(III) are associated with surface terminating groups, while Ti(IV) is associated with TiO_2. MXene/HPW12 presents less intensive Ti(II) peaks and more intensive Ti (III) peaks than MXene, implying the inclusion of the small amount of HPW12 changed the valence of Ti. HPW12 is anchored on MXene through chemical bonds. By contrast, the Ti 2p spectrum of MXene/AC/TEAPW12 does not show such significant change except for stronger Ti(IV) peaks, which should be ascribed to the fact that AC is just physically constrained among MXene nanosheets and TEAPW12 are pre-immobilized on AC. The stronger Ti(IV) peaks in MXene/HPW12 and MXene/AC/TEAPW12 must be associated with the slight oxidation due to the high-power probe-sonication. We also collected high-resolution spectra from 25 to 45 eV to investigate the W 4f orbital in hybrid materials. However, since the binding energy of Ti 3p is very close to W 4f, the W $4f^{7/2}$ and $4f^{5/2}$ peaks are deformed. Nonetheless, it is still possible to discern the two main peaks at 36.1 and 38.2 eV, agreeing well with W(VI) $4f^{7/2}$ and $4f^{5/}2$ peaks in PW12 (Fig. S2d).

HAADF-STEM is an effective method to investigate the dispersion of heavy atoms, particularly the PW12 clusters. Fig. 4a-d present HAADF-STEM images of pure MXene and these hybrid samples. The corresponding HR-TEM images are presented in Fig. S3. Under HAADF-STEM, MXene (Fig. 4a) presents a homogeneous texture, while MXene/HPW12 (Fig. 4b) is slightly different. In some areas, the nanosheets are covered by a thin, bright layer, corresponding to PW12 confirmed by EDX (Fig. S4). We conclude that MXene is not an effective substrate for dispersing PW12 clusters because aggregation happens even in low loading mass. On the other hand, the dispersion states of PW12 clusters in triple hybrid materials MXene/AC/HPW12 (Fig. 4c) and MXene/AC/TEAPW12 (Fig. 4d) are quite different from the MXene/HPW12. The bright dots, around 1 nm (as confirmed by EDX element mapping and line scan in Fig. S5), spread homogeneously on the substrate, indicating that the PW12 clusters are well-dispersed at the nanoscale. Fig. 4e-f present the STEM image and the EDX element mapping in an extended area, in which we can discern the MXene nanosheets surrounding the AC particles loaded with PW12 clusters. The SAED patterns (Fig. S6) prove the triple hybrid materials have mixed phases: crystallized MXene, amorphous AC and uncrystallized PW12 clusters. This is in good agreement with the fact that MXene/AC/HPW12 and MXene/AC/TEAPW12 do not show any diffraction peaks other than those of MXene in XRD.

With the images of SEM and STEM, we illustrate how the three components combine in MXene/AC/TEAPW12 (Fig. 5). First, the PW12 nanoclusters are anchored on microporous AC matrix and dispersed at nanoscale. Then, the PW12-anchored AC particles mix with flexible MXene nanosheets and stack together under vacuum-assisted filtration. Finally, we obtain the PW12-anchored AC wrapped by MXene nanosheets.

Cyclic voltammograms were carried out to characterize the electrochemical properties of the materials, as well as to determine the capacitance of the various electrodes studied and to analyze the energy storage mechanisms. The CV of MXene in 1 M TEABF4 in acetonitrile (Fig. 6a) is predominantly capacitive (ideally rectangular shape) but superposed a pair of broad redox waves. The reduction wave centred at –1.75 V vs. Ag/Ag^+ must be ascribed to the intercalation of TEA^+. The corresponding oxidation peak, centred at –1.48 V vs. Ag/Ag^+, is broader and weaker, indicating the

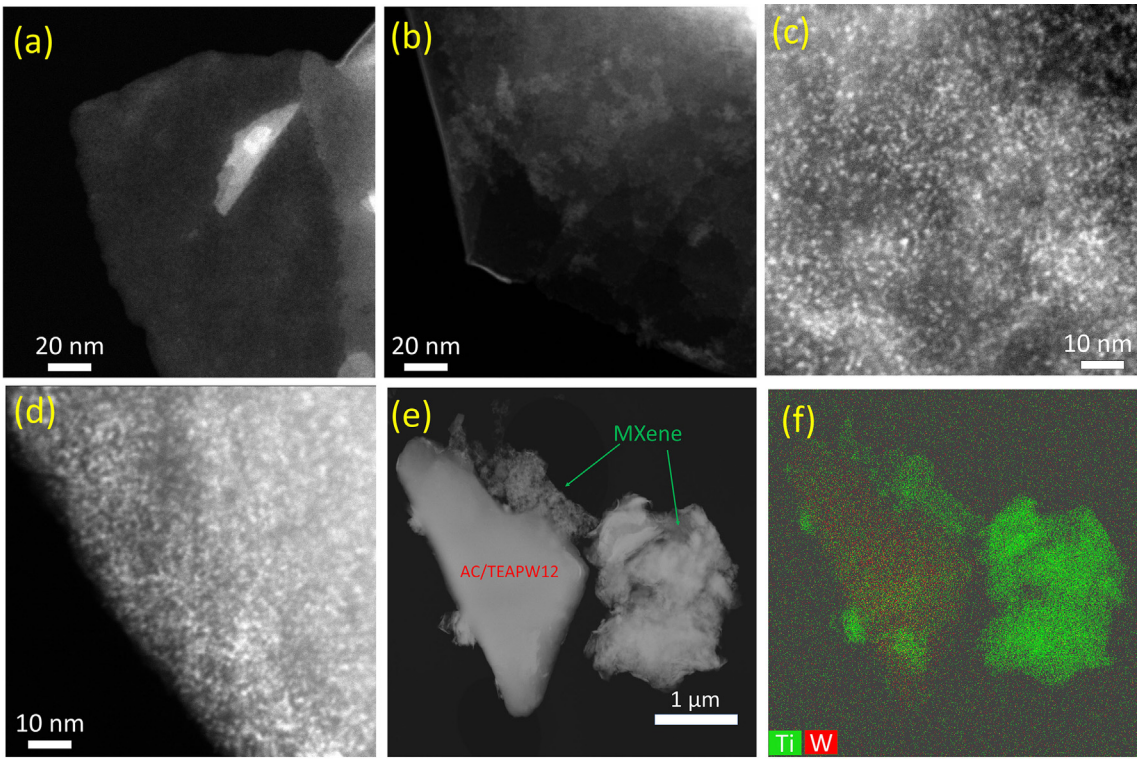

Fig. 4. HAADF-STEM images of (a) MXene, (b) MXene/HPW12, (c) MXene/AC/HPW12 and (d) MXene/AC/TEAPW12. (e) STEM image at low magnification and (f) the corresponding element mapping of MXene/AC/TEAPW12.

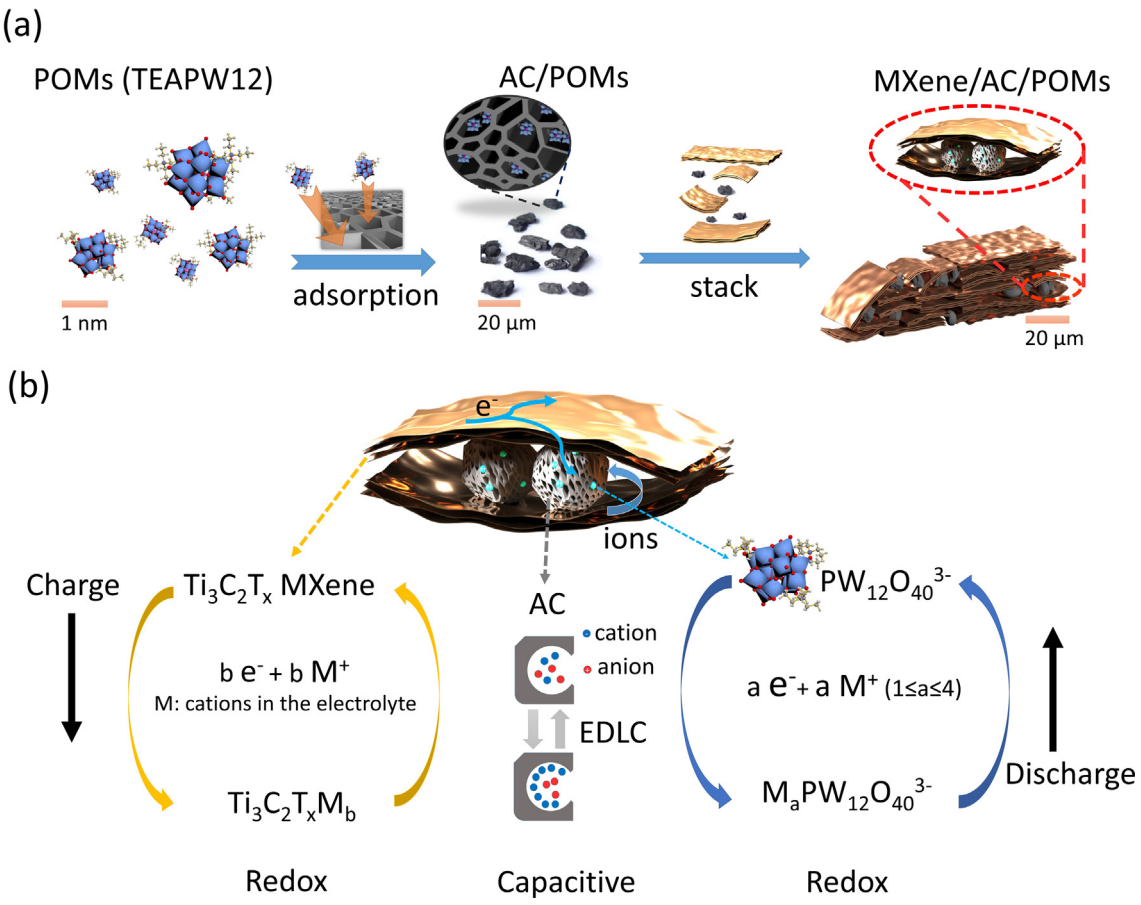

Fig. 5. Schematic illustration of the combination of TEAPW12, AC and MXene. (b) Schematic illustration of the working mechanism of MXene/AC/TEAPW12.

intercalation–deintercalation process is not 100% reversible. This agrees well with the XRD patterns of cycled MXene, in which we observe a significant shifting of (002) peak to low angle (Fig. S7). In the CV of MXene/HPW12 (Fig. 6a), besides the broad waves from MXene, we can discern some new small peaks from PW12 clusters. Since the loading mass of HPW12 is very low, these peaks are weak and their contribution to the capacitance is not very substantial.

The CV of MXene/AC/TEAPW12 (Fig. 6b) mainly shows four pairs of redox waves, similar to AC/TEAPW12[33]. Since TEAPW12 is immobilized on AC in advance, MXene/AC/TEAPW12 presents redox waves at the same positions. Fig. 5(b) illustrates how the triple hybrid MXene/AC/TEAPW12 works. The MXene nanosheets and porous AC particles construct the framework for electron flow. The hierarchical porous structure facilitates ion diffusion. As a result, all three components contribute to electrochemical energy storage: MXene and TEAPW12 store charges through reversible redox reactions; AC store charges through electric double-layer capacitance.

On the other hand, the situation is more complicated for MXene/AC/HPW12. The CV of MXene/AC/HPW12 (Fig. 6b) shows more than six pairs of redox waves. In principle, PW12 clusters only present three or four pairs of redox waves in this potential range (more redox pairs are possible in a wider potential range, but they are not 100% reversible). The extra redox waves must be associated with different anchoring states: PW12 clusters anchoring on AC; and PW12 clusters anchoring on MXene (The classification of these redox waves is presented in Fig. S8a-c).

To investigate the energy storage mechanism, we carried out CVs at various scan rates (Fig. S9). The dependence of the current response on the scan rate can provide insights into the charge-storage mechanism according to Eq9 as suggested by John Wang et al. [52]:

$$\frac{i(V)}{v^{1/2}} = k_1 v^{1/2} + k_2 \tag{9}$$

where $i(V)$ is the current at the given potential V, v is the scan rate. k_1 is a variable characterizing the contribution from surface capacitive processes (e.g. pseudocapacitance, electric double layer capacitance), and k_2 is the other variable representing the contribution from diffusion-controlled processes (e.g. intercalation–deintercalation, sluggish redox reactions) at a given potential. k_1 and k_2 can be determined by a linear fitting of Eq9.

Fig. 6c shows the contribution of the diffusion-controlled process versus the surface capacitive process to the overall capacitance of MXene/AC/TEAPW12 from 0.2 to 2 mV s^{-1}. The surface capacitive process dominates the energy storage process in the whole range. At 0.2 mV s^{-1}, the surface capacitive process accounts for 78.9% of total capacitance; when the scan rate rises to 2 mV s^{-1}, this ratio increases to 91%. With the rise of the scan rate, the contribution of surface capacitance increases, revealing that the surface capacitive process prevails at faster scan rates. This trend is common in many other hybrid materials[53,54]. MXene/AC/TEAPW12 maintains a higher surface capacitive contribution in the whole range, mainly benefiting from the excellent dispersion of PW12 clusters.

Fig. 6d presents the gravimetric capacitance of MXene, MXene/HPW12, MXene/AC/HPW12 and MXene/AC/TEAPW12 in 1 M TEABF4 in acetonitrile at various scan rates. MXene and MXene/HPW12 almost deliver the exact equivalent gravimetric capacitance because the loading of PW12 on MXene/HPW12 is very low. MXene/AC/HPW12 and MXene/AC/TEAPW12 exhibit significantly higher gravimetric capacitance, thanks to AC with high gravimetric capacitance. Compared with the hybrid material

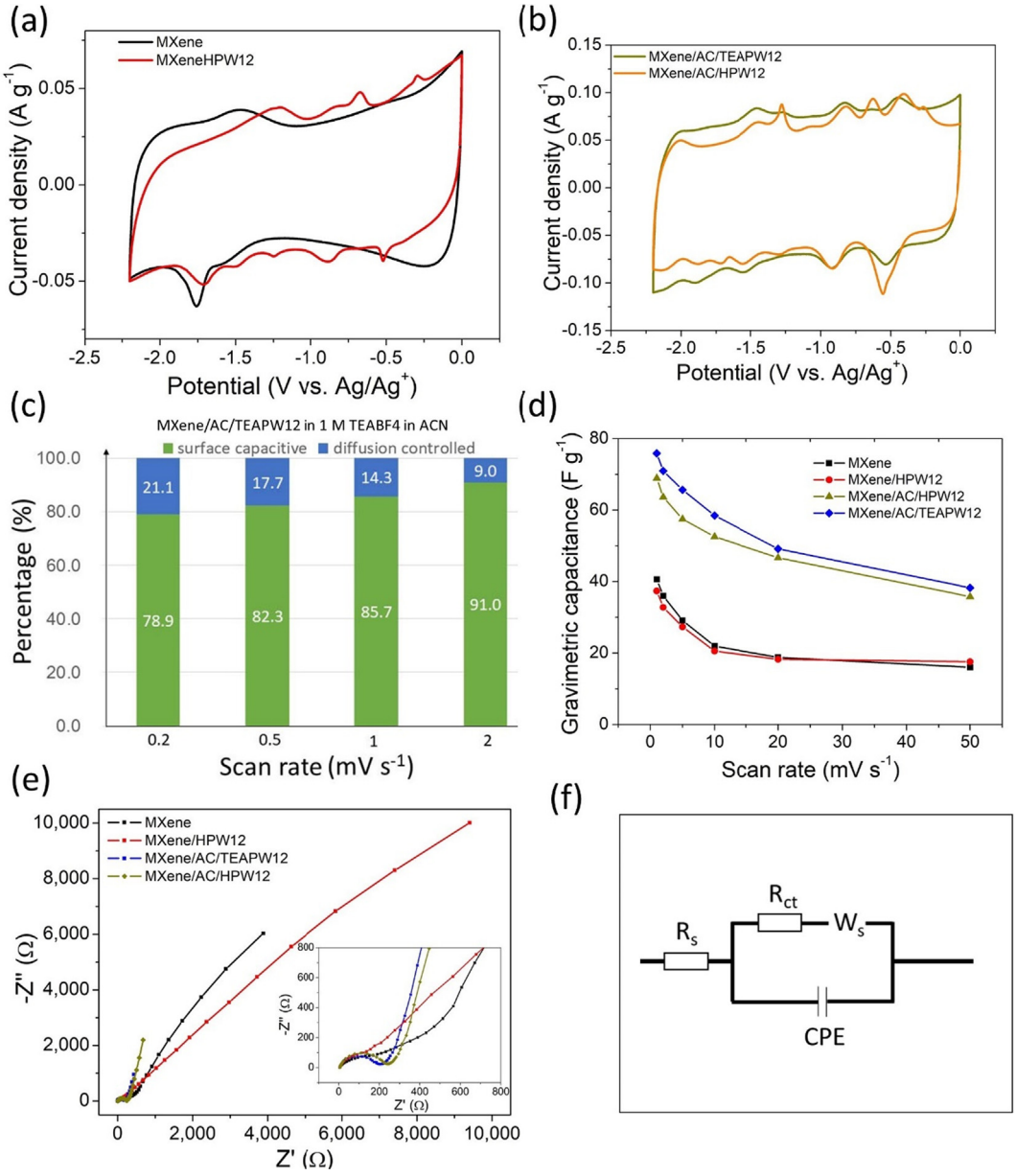

Fig. 6. (a) Cyclic voltammograms of MXene and MXeneHPW12 at 1 mV s^{-1} in 1 M TEABF4 acetonitrile. (b) Cyclic voltammograms of MXene/AC/HPW12 and MXene/AC/TEAPW12 at 1 mV s^{-1} in 1 M TEABF4 acetonitrile. (c) Surface capacitive contribution and diffusion-controlled contribution at various scan rates. (d) Gravimetric capacitance of MXene, MXene/HPW12, MXene/AC/HPW12 and MXene/AC/TEAPW12 at various scan rates. (e) Electrochemical impedance spectra of MXene, MXene/HPW12, MXene/AC/HPW12 and MXene/AC/TEAPW12. (f) Equivalent circuit for fitting impedance spectra.

MXene/AC of the same weight ratio (MXene/AC 1:1, 88F g^{-1} at 0.1 A g^{-1}[16], or 77F g^{-1} at 1 mV s^{-1}(Fig. S10)), MXene/AC/TEAPW12 could deliver the equivalent gravimetric capacitance. The addition of TEAPW12 does not improve the gravimetric capacitance due to the large molecular weight of PW12 clusters (>2800 g mol^{-1}). On the other hand, as other studies show, the anchoring of TEAPW12 can improve the volumetric capacitance, instead of the gravimetric capacitance in the same electrolyte[33]. Due to the porous nature of AC, MXene/AC delivers 33% lower volumetric capacitance than that of MXene[16]. In contrast, in our study, the volumetric capacitance of MXene/AC/TEAPW12 is only around 10% lower than pristine MXene (Fig. S10), but much higher than MXene/AC[16], AC/TEAPW12[33] and AC[33].

To investigate the electrochemical response as well as diffusion properties of the triple hybrids, we carried out impedance tests (Fig. 6e). All the spectra are fitted by a modified Randles circuit (Fig. 6f). The fitted values are presented in Table S4. The intercepts at the very high-frequency region represent equivalent series resistance (R_s), which is a combination of the ionic resistance of the electrolyte, the intrinsic resistance of the active materials, and the contact resistance at the active material/current collector interface. Since all the electrodes were characterized in the same setup, their R_s are similar. The arc at high frequency represents charge-transfer resistance R_{ct}. The following transitory parts between the semicircles and the final linear parts represent the Warburg impedance, which is associated with mass transfer (diffusion). The R_{ct} of MXene and MXene/HPW12 are smaller (around 50%) than MXene/AC/HPW12 and MXene/AC/TEAPW12, but the diffusion impedance values are significantly larger (5 times), revealing that different steps restrict the charge store process. In MXene and MXene/HPW12, due to the high electronic conductivity of MXene nanosheets, the active sites which have already been

exposed to the electrolyte can carry out the charge transfer process quickly, leading to a relatively smaller R_{ct}. After that, ions have to diffuse through the slits between nanosheets, or even insert layers to reach the active sites. As a result, their diffusion impedance values are extremely large. By contrast, MXene/AC/HPW12 and MXene/AC/TEAPW12 have larger R_{ct} due to the inferior electronic conductivity of AC, but the diffusion is greatly promoted thanks to the hierarchical porous structure.

In general, the electrochemical performance of any electrode is related to its thickness, especially for MXenes. Normally, thicker MXene electrodes lead to remarkably lower volumetric capacitance[4]. In our case, on the contrary, the increased porosity of our hybrid material leads to a thicker electrode (as shown by SEM) but with improved capacitance. We chose to compare pristine MXene with hybrid electrodes keeping their masses (areal densities) comparable, rather than their thicknesses.

The combination of the three components has a synergistic effect in that several merits are merged in the MXene/AC/TEAPW12 triple hybrid. We attempted to estimate the overall capacitance contributed from each component according to the composition and individual specific capacitance. For instance, at 1 mV s^{-1} the gravimetric capacitance of MXene/AC/TEAPW12, MXene and AC/TEAPW12 is 76F g^{-1}, 40F g^{-1} and 90F g^{-1}, respectively. Since MXene and AC/TEAPW12 each account for half the mass of MXene/AC/TEAPW12, a MXene:AC/TEAPW12 = 1:1 mixture would have a gravimetric capacitance of 65F g^{-1}, lower than the MXene/AC/TEAPW12 hybrid material. The extra capacitance must be ascribed to the fact that AC/TEAPW12 promotes the porous properties of MXene, which is a part of the synergistic effect. Furthermore, the MXene provides a conductive substrate with high volumetric capacitance. AC provides a microporous matrix for TEAPW12 anchoring, and also contributes to high gravimetric capacitance. TEAPW12 clusters could be nanodispersed and durably anchored on AC, providing extra-fast reversible redox reactions not limited by diffusion, and compensating the sacrificed volumetric capacitance due to the addition of AC. Finally, we were able to obtain a well-balanced triple hybrid material with both high gravimetric and volumetric capacitances in a conventional organic electrolyte.

The capacitance of MXene in organic electrolytes can be improved by fine tuning of the ions used in the electrolyte. Thus, EMIMTFSI has flatter cations than TEABF4, and the cations could intercalate into MXene more easily. Accordingly, MXene can deliver higher capacitance in the EMIMTFSI/acetonitrile electrolyte [8]. We compared the electrochemical behaviors of MXene/AC/HPW12 and MXene/AC/TEAPW12 in 1 M EMIMTFSI in acetonitrile and 1 M TEABF4 in acetonitrile (Fig. 7a). The current densities of the CVs in 1 M EMIMTFSI in acetonitrile are remarkably higher than those in 1 M TEABF4 in acetonitrile, indicating a larger capacitance. The CVs of MXene/AC/HPW12 and MXene/AC/TEAPW12 show more than one pair of redox waves in 1 M EMIMTFSI in acetonitrile, implying the PW12 clusters are still redox active in this electrolyte. Fig. 7b presents the gravimetric capacitance of MXene, MXene/AC/HPW12 and MXene/AC/TEAPW12 at various scan rates. MXene/AC/TEAPW12 still delivers the largest gravimetric capacitance (102 F g^{-1} at 1 mV s^{-1}) among the three, almost double that of MXene (52 F g^{-1} at 1 mV s^{-1}), and also higher than the gravimetric capacitance of MXene/AC/TEAPW12 (76 F g^{-1} at 1 mV s^{-1}) in 1 M TEABF4 in acetonitrile. The enhancement of capacitance derives from the cation intercalation–deintercalation in the energy storage process. Since the cation intercalation–deintercalation is usually diffusion-controlled, we carried out the CVs at various scan rates to analyze the contribution from these two mechanisms.

Fig. 7c presents the contribution of the diffusion-controlled and surface capacitive processes from 0.2 mV s^{-1} to 2 mV s^{-1}. The surface capacitive process still dominates the energy storage in the whole range, but the diffusion-controlled process starts to play a bigger role. At 0.2 mV s^{-1} ,the diffusion-controlled process accounts for 43.5%, more than double that in 1 M TEABF4 in acetonitrile. The remarkably increased ratio of the diffusion-controlled contribution proves the deeper involvement of cation intercalation–deintercalation in MXene, thus, MXene and MXene/AC/TEAPW12 could deliver more capacitance in 1 M EMIMTFSI in acetonitrile.

We charge-discharged MXene/AC/TEAPW12 for 10,000 cycles in both electrolytes (Fig. 7d) and ran CVs before and after cycling (Fig. 7e and f). MXene/AC/TEAPW12 shows excellent cycle stability in 1 M TEABF4 acetonitrile. Its capacitance almost remains the same after 10,000 cycles. Furthermore, the CV after 10,000 cycles exhibits four pairs of redox waves. Their current densities even stay the same, indicating the anchoring and redox activities of PW12 clusters do not change. The excellent cycle stability and long-term anchoring of PW12 clusters must be ascribed to the AC matrix, which has been proved to be an ideal substrate for anchoring POMs[35,39,43]. In contrast, the in-situ growth MXene/TEAPW12 show much worse cycle stability (Fig. S8d) in the same electrolyte. The redox waves almost disappear after 1000 cycles (Fig. S8e). Other previously reported MXene/POM hybrid materials cannot give very long-term cycle stability[32]. Thus, AC is the key to the excellent cyclic performance of the triple hybrid materials. In 1 M EMIMTFSI in acetonitrile, the capacitance of MXene/AC/TEAPW12 increases by 7% after 10,000 cycles, which could be associated with the expanded interlayer distance due to cation intercalation during cycling[11,55]. However, the deep cation intercalation is not problem-free. Firstly, this cation intercalation–deintercalation is not 100% reversible, which is reflected by the fact that in 1 M EMIMTFSI in acetonitrile the Coulombic efficiency is lower because more cations involve in intercalation. Moreover, the long-term, repeating intercalation–deintercalation could damage the microstructure and worsen the conductivity, which is revealed by CVs (Fig. 7f). The electrode after 10,000 cycles suffers larger resistance. The electrochemical impedance spectra further confirm it.

Fig. 7g compares the impedance spectra of MXene/AC/TEAPW12 before and after cycled in 1 M TEABF4 in acetonitrile. The the spectrum was fitted by the same equivalent circuit (Fig. 6f) and the fitting values are presented in Table S5. The two spectra almost overlap. The zoom-in figure (Fig. 7g inset) presents the slight different, in which we can only discern the slightly larger arc, corresponding to R_{ct}. By contrast, the impedance spectrum of MXene/AC/TEAPW12 cycled in 1 M EMIMTFSI in acetonitrile (Fig. 7h) is significantly different from the fresh one. The intercept on X-axis (representing R_s) stays the same, but the arc (R_{ct}) is remarkably larger and the followed linear transition zoom (related to diffusion impedance) is remarkably longer, revealing that the charge-transfer and diffusion processes are impeded in the cycled electrode. The impedance spectra confirm that long-term intercalation–deintercalation in 1 M EMIMTFSI in acetonitrile could damage the microstructure, hindering ion diffusion and leading to high resistance.

Table 3 compares the capacitive performance of the triple hybrid material MXene/AC/TEAPW12 and the double hybrid materials MXene/AC, AC/TEAPW12 and MXene/TEAPW12 in 1 M TEABF4 in acetonitrile, which demonstrates the superiority of the triple hybrid material over double hybrid materials. Compared with MXene/AC and AC/TEAPW12, MXene/AC/TEAPW12 shows enhanced volumetric capacitance without sacrificing gravimetric capacitance and cycle stability. Meanwhile, the defects of MXene/TEAPW12, i.e. poor cycle stability and low gravimetric capacitance, are overwhelmed in MXene/AC/TEAPW12.

We assembled asymmetric supercapacitors to compare the potential application of the MXene/AC/TEAPW12 triple hybrid

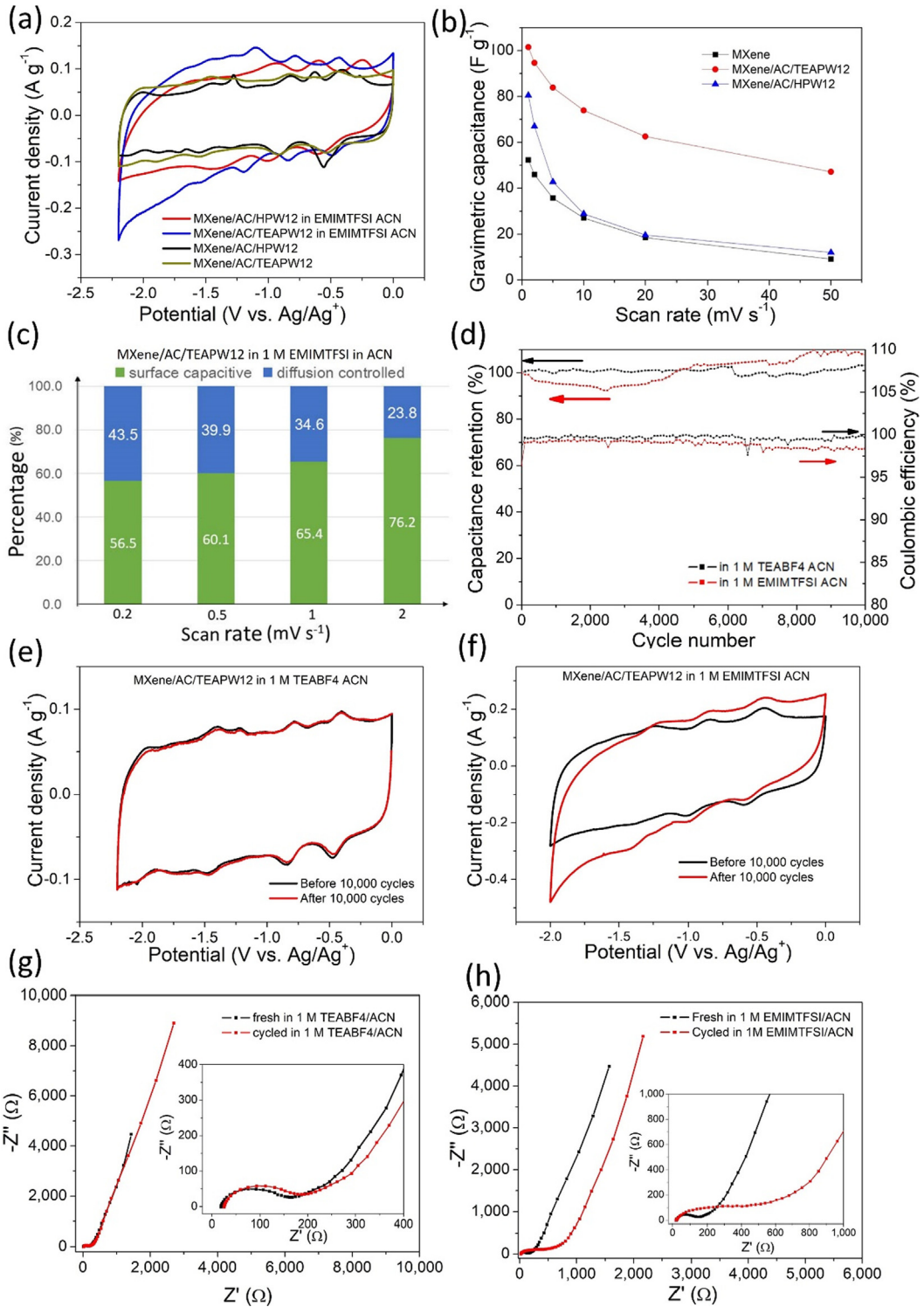

Fig. 7. (a) CVs of MXene/AC/HPW12 and MXene/AC/TEAPW12 at 1 mV s^{-1} in 1 M TEABF4 in acetonitrile or 1 M EMIMTFSI in acetonitrile; (b) Gravimetric capacitance of MXene, MXene/AC/HPW12 and MXene/AC/TEAPW12 in 1 M EMIMTFSI in acetonitrile; (c) Diffusion-controlled contribution and surface capacitive contribution at various scan rates; (d) Cycling stability test: capacitance retention and Coulombic efficiency of MXene/AC/TEAPW12 in the two electrolytes (current density: 2 A g^{-1}). (e) CVs of MXene/AC/TEAPW12 in 1 M TEABF4 in acetonitrile before and after cycling; (f) CVs of MXene/AC/TEAPW12 in 1 M EMIMTFSI in acetonitrile before and after cycling. Electrochemical impedance spectra of MXene/AC/TEAPW12 before and after cycling in (g) 1 M TEABF4 in acetonitrile and (h) 1 M EMIMTFSI in acetonitrile.

materials (AC//MXene/AC/TEAPW12) and pristine MXene (AC//MXene) in full-cell. The conventional AC electrodes served as the positive electrode. 1 M TEABF4 in acetonitrile served as the electrolyte. The details about preparing AC electrodes and charge balance calculation are presented in supplementary materials.

Fig. 8a presents the CVs of the positive (AC) and negative (MXene/AC/TEAPW12) electrodes in the respective potential range, in which the negative electrode is charged to –2.2 V, and the positive electrode is charged to + 0.5 V. As a result, a voltage window of 2.7 V can be achieved in the full cell. Cyclic polarization (CP) was

Table 3
Comparison of the capacitive performance of the triple hybrid material MXene/AC/TEAPW12 and the double hybrid materials MXene/AC, AC/TEAPW12 and MXene/TEAPW12.

	Gravimetric capacitance	Volumetric capacitance	Capacitance retention	Reference
MXene/AC/TEAPW12	87F g^{-1} at1 mV s^{-1}	76F cm^{-3} at 1 mV s^{-1}	102% after 10,000 cycles	this work
MXene/AC[a]	88F g^{-1} at 0.1 A g^{-1}	30F cm^{-3} at 0.1 A g^{-1}	92% after 10,000 cycles	[16]
AC/TEAPW12[b]	92F g^{-1} at1 mV s^{-1}	64F cm^{-3} at 1 mV s^{-1}	93% after 10,000 cycles	[33]
MXene/TEAPW12	36F g^{-1} at1 mV s^{-1}	120F cm^{-3} at 1 mV s^{-1}	80% after 1,000 cycles	this work

a, MXene account for 50 wt% in MXene/AC. b, it is not a free-standing electrode, the mass of the binder, conductive additive and current collector are not included in calculating the gravimetric capacitance.

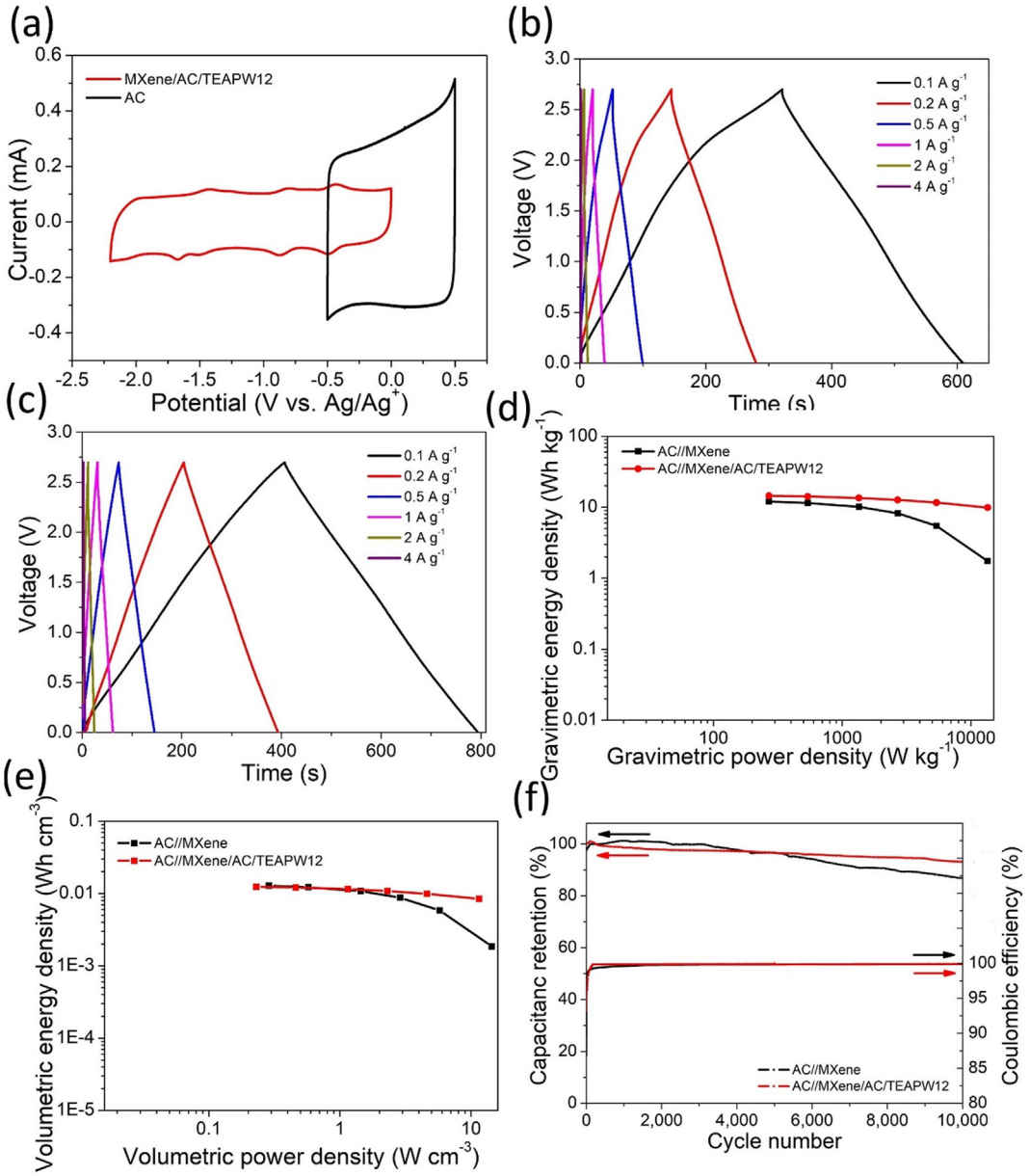

Fig. 8. (a) CVs of the positive and negative electrodes in AC//MXene/AC/TEAPW12 asymmetric cell. Galvanostatic charge–discharge curves of (b) AC//MXene and (c) AC//MXene/AC/TEAPW12 cells at various current densities. (d) Gravimetric and (e) volumetric Ragone plot of AC//MXene and AC//MXene/AC/TEAPW12 cell. (f) Cycling stability test: capacitance retention and Coulombic efficiency of AC//MXene and AC//MXene/AC/TEAPW12 cell during charge–discharge at 1 A g^{-1} for 10,000 cycles.

carried out on both asymmetric cells at various scan rates (from 2 mV s^{-1} to 1 V s^{-1}, Fig. S11a-d). The CP curves of AC//MXene/AC/TEAPW12 present several weak waves during the charging and discharging processes, deriving from the redox reaction of TEAPW12. At high scan rates (>100 mV s^{-1}), the CP curves of AC//MXene/AC/TEAPW12 remain rectangular while those of AC//MXene do not, indicating the better rate capability of AC//MXene/AC/TEAPW12 cell. The specific capacitance normalized by the total mass of two electrodes at various scan rates is presented in Fig. S11e.

Galvanostatic charge–discharge (GCD) was carried out to evaluate the performance of the asymmetric cells in practical application. The GCD curves of AC//MXene (Fig. 8b) diverge from the ideal triangular shape due to the sluggish intercalation–deintercala

tion of cations in MXene. In contrast, the GCD curves of AC//MXene/AC/TEAPW12 (Fig. 8c) are triangular, which agrees with the previous single electrode analysis: MXene/AC/TEAPW12 mainly stores charges through surface capacitive processes. The gravimetric capacitance of the asymmetric cells at various current densities or scan rates is presented in Fig. S11f. The AC//MXene/AC/TEAPW12 surpasses AC//MXene, especially at high rates.

Fig. 8d-e present Ragone plots normalized by the total mass or volume of two electrodes, respectively. The data in these plots demonstrate that the hybrid AC//MXene/AC/TEAPW12 features higher gravimetric energy densities as well as higher volumetric energy densities compared with AC//MXene. In the gravimetric Ragone plot, AC//MXene/AC/TEAPW12 delivers an energy density of 14.2 Wh kg^{-1} at a power density of 540 W kg^{-1}, 25% higher than AC//MXene. At high rates, the superiority of AC//MXene/AC/TEAPW12 is remarkable. The energy density of AC//MXene/AC/TEAPW12 is 5.6 times that of AC//MXene at 13.5 kW kg^{-1}. Meanwhile, even normalized by volume, AC//MXene/AC/TEAPW12 does not fall behind. At low power densities, AC//MXene/AC/TEAPW12 delivers almost equivalent volumetric energy densities (0.012 Wh cm^{-3} at 0.23 W cm^{-3}) compared with AC//MXene (0.013 Wh cm^{-3} at 0.29 W cm^{-3}). At high power densities, AC//MXene/AC/TEAPW12 outperforms AC//MXene significantly as well (8.5 mWh cm^{-3} at 11.5 W cm^{-3} for AC//MXene/AC/TEAPW12, 1.9 mWh cm^{-3} at 14.4 W cm^{-3} for AC//MXene). The advantage of AC//MXene/AC/TEAPW12 lies in its excellent rate capability of the asymmetric cell that must be associated with the merits of the hybrid MXene/AC/TEAPW12 electrode. That is, AC particles suppress restacking of MXene flakes, promoting ion diffusion and TEAPW12 clusters are dispersed homogeneously on AC, able to conduct fast reversible redox reaction. Both of them lead to excellent rate capability.

We also charge-discharged both asymmetric cells at 1 A g^{-1} for 10,000 cycles to evaluate their cycle stability (Fig. 8f). As we have proved the excellent cycle stability of MXene/AC/TEAPW12 single electrode in a wide potential range (Fig. 5d-e), the AC//MXene/AC/TEAPW12 cell is expected to have good cycle stability. After 10,000 cycles, 92% of its initial capacitance remained and although the AC//MXene cell also exhibits good cyclability, its cycle stability decreased faster (88% remaining after 10,000 cycles). The Coulombic efficiencies of both cells increased at the first few cycles, then stayed over 99.5%. We performed post-mortem analyses (Fig. S12) on the cycled MXene/AC/TEAPW12 electrode. The morphology of the cycled MXene/AC/TEAPW12 is as same as the fresh one, and the EDX spectrum indicates the existence of W. The long-term cycling did not damage the porous structure and the anchoring of POMs. The good cycle stability can be ascribed to both the stability of active materials and the proper charge balance and the fact that the potential of the two electrodes is not taken beyond the stable potential window of the electrolyte.

4. Conclusion

In this work, we did design and prepared for the first time a MXene/activated carbon (AC)/polyoxometalate(POM) hybrid material which shows synergic effects, making it possible an effective, functional and long-lasting incorporation of POMs to MXene. Our work also has shown how to modulate the properties of a final electrode by choosing wisely the properties of the components and the final composition. Thus, MXene plays the role of a conductive scaffold, provides high volumetric capacitance and allows for fabricating free-standing electrodes. AC serves as the matrix for anchoring POMs, provides high gravimetric capacitance and ensures good cyclic performance. POMs provide extra fast reversible redox activity and enhance volumetric capacitance. As-prepared MXene/AC/TEAPW12 triple hybrid material delivered much larger gravimetric capacitance ((87 F g^{-1} at 1 mV s^{-1})) than MXene (40 F g^{-1} at 1 mV s^{-1}) in conventional organic electrolyte without sacrificing much volumetric capacitance (less than 10%). Even compared with MXene/AC of the same mass ratio, the gravimetric capacitance of MXene/AC/TEAPW12 was almost equivalent and the volumetric capacitance was 1.5 times higher. The capacitive performance can be further improved by replacing spherical TEA with flat EMIM cations in the electrolyte. The asymmetric cell AC//MXene/AC/TEAPW12 outperformed AC//MXene cell concerning both gravimetric (4.6 times higher at 13.5 kW kg^{-1}) and volumetric energy densities (3.5 times higher at around 13 W cm^{-3}) and featured very good cycle stability (92% after 10,000 cycles). The work shed light on the synergic effects in the triple hybrid materials. We can further improve gravimetric and/or volumetric capacitance by using other POMs, fine-tuning composition ratios, etc.

CRediT authorship contribution statement

Jun-Jie Zhu: Methodology, Conceptualization, Formal analysis, Investigation, Writing – original draft. **Avireddy Hemesh:** Resources, Conceptualization, Formal analysis, Project administration. **Jordi Jacas Biendicho:** Software, Writing – review & editing. **Luis Martinez-Soria:** Resources, Data curation. **Daniel Rueda-Garcia:** Formal analysis, Resources. **Joan Ramon Morante:** Writing – review & editing, Funding acquisition. **Belen Ballesteros:** Formal analysis, Data curation. **Pedro Gomez-Romero:** Writing – review & editing, Supervision, Funding acquisition.

Declaration of Competing Interest

The authors declare that they have no known competing financial interests or personal relationships that could have appeared to influence the work reported in this paper.

Acknowledgements

Partial funding from Ministry of Science, Innovation and Universities (MCIU), the State Research Agency (AEI) and the European Regional Development Fund (FEDER) (grant RTI2018-099826-B-I00) and AGAUR (2017 SGR 00870, 2017 SGR 1246) are gratefully acknowledged. ICN2 and IREC are funded by the CERCA programme / Generalitat de Catalunya, and ICN2 is also supported by the Severo Ochoa Centres of Excellence programme, funded by the Spanish Research Agency (AEI, grant no. SEV-2017-0706). J.J Z. acknowledges his scholarship (No. 201806370211) under China Scholarship Council. We thank Haizea Rodriguez Sagasti for help with the programming to calculate the contribution from different energy storage mechanisms. This work has been carried out within the framework of doctoral program (PhD) of Material Science (Department of Physics) of Universitat Autònoma de Barcelona (UAB).

Appendix A. Supplementary material

Supplementary data to this article can be found online at https://doi.org/10.1016/j.jcis.2022.04.170.

References

[1] D.P. Dubal, O. Ayyad, V. Ruiz, P. Gomez-Romero, Hybrid energy storage: the merging of battery and supercapacitor chemistries, Chem. Soc. Rev. 44 (7) (2015) 1777–1790, https://doi.org/10.1039/c4cs00266k.
[2] C.E. Shuck, Y. Gogotsi, Taking MXenes from the lab to commercial products, Chem. Eng. J. 401 (2020), https://doi.org/10.1016/j.cej.2020.125786 125786.

[3] M.R. Lukatskaya, S. Kota, Z. Lin, M.-Q. Zhao, N. Shpigel, M.D. Levi, J. Halim, P.-L. Taberna, M.W. Barsoum, P. Simon, Y. Gogotsi, Ultra-high-rate pseudocapacitive energy storage in two-dimensional transition metal carbides, Nat. Energy 2 (8) (2017) 17105, https://doi.org/10.1038/nenergy.2017.105.
[4] M. Ghidiu, M.R. Lukatskaya, M.Q. Zhao, Y. Gogotsi, M.W. Barsoum, Conductive two-dimensional titanium carbide 'clay' with high volumetric capacitance, Nature 516 (7529) (2014) 78–81, https://doi.org/10.1038/nature13970.
[5] M.Q. Zhao, C.E. Ren, Z. Ling, M.R. Lukatskaya, C. Zhang, K.L. Van Aken, M.W. Barsoum, Y. Gogotsi, Flexible MXene/carbon nanotube composite paper with high volumetric capacitance, Adv. Mater. 27 (2) (2015) 339–345, https://doi.org/10.1002/adma.201404140.
[6] M.R. Lukatskaya, O. Mashtalir, C.E. Ren, Y. Dall'Agnese, P. Rozier, P.L. Taberna, M. Naguib, P. Simon, M.W. Barsoum, Y. Gogotsi, Cation Intercalation and High Volumetric Capacitance of Two-Dimensional Titanium Carbide, Science 341 (6153) (2013) 1502–1505.
[7] H. Avireddy, B.W. Byles, D. Pinto, J.M. Delgado Galindo, J.J. Biendicho, X. Wang, C. Flox, O. Crosnier, T. Brousse, E. Pomerantseva, J.R. Morante, Y. Gogotsi, Stable high-voltage aqueous pseudocapacitive energy storage device with slow self-discharge, Nano Energy 64 (2019), https://doi.org/10.1016/j.nanoen.2019.103961 103961.
[8] Y. Dall'Agnese, P. Rozier, P.-L. Taberna, Y. Gogotsi, P. Simon, Capacitance of two-dimensional titanium carbide (MXene) and MXene/carbon nanotube composites in organic electrolytes, J. Power Sources 306 306 (2016) 510–515.
[9] Z. Lin, D. Barbara, P.-L. Taberna, K.L. Van Aken, B. Anasori, Y. Gogotsi, P. Simon, Capacitance of Ti3C2Tx MXene in ionic liquid electrolyte, J. Power Sources 326 (2016) 575–579, https://doi.org/10.1016/j.jpowsour.2016.04.035.
[10] Q. Fan, R. Zhao, M. Yi, P. Qi, C. Chai, H. Ying, J. Hao, Ti3C2-MXene composite films functionalized with polypyrrole and ionic liquid-based microemulsion particles for supercapacitor applications, Chem. Eng. J. 428 (2022), https://doi.org/10.1016/j.cej.2021.131107 131107.
[11] J. Luo, W. Zhang, H. Yuan, C. Jin, L. Zhang, H. Huang, C. Liang, Y. Xia, J. Zhang, Y. Gan, X. Tao, Pillared Structure Design of MXene with Ultralarge Interlayer Spacing for High-Performance Lithium-Ion Capacitors, ACS Nano 11 (3) (2017) 2459–2469, https://doi.org/10.1021/acsnano.6b07668.
[12] X. Wang, T.S. Mathis, K. Li, Z. Lin, L. Vlcek, T. Torita, N.C. Osti, C. Hatter, P. Urbankowski, A. Sarycheva, M. Tyagi, E. Mamontov, P. Simon, Y. Gogotsi, Influences from solvents on charge storage in titanium carbide MXenes, Nat. Energy 4 (3) (2019) 241–248, https://doi.org/10.1038/s41560-019-0339-9.
[13] X. Wang, S. Kajiyama, H. Iinuma, E. Hosono, S. Oro, I. Moriguchi, M. Okubo, A. Yamada, Pseudocapacitance of MXene nanosheets for high-power sodium-ion hybrid capacitors, Nat. Commun. 6 (2015) 6544, https://doi.org/10.1038/ncomms7544.
[14] J. Luo, C. Fang, C. Jin, H. Yuan, O. Sheng, R. Fang, W. Zhang, H. Huang, Y. Gan, Y. Xia, C. Liang, J. Zhang, W. Li, X. Tao, Tunable pseudocapacitance storage of MXene by cation pillaring for high performance sodium-ion capacitors, J. Mater. Chem. A 6 (17) (2018) 7794–7806, https://doi.org/10.1039/c8ta02068j.
[15] S. Kajiyama, L. Szabova, H. Iinuma, A. Sugahara, K. Gotoh, K. Sodeyama, Y. Tateyama, M. Okubo, A. Yamada, Enhanced Li-Ion Accessibility in MXene Titanium Carbide by Steric Chloride Termination, Adv. Energy Mater. 7 (9) (2017) 1601873, https://doi.org/10.1002/aenm.201601873.
[16] L.Y. Yu, L.F. Hu, B. Anasori, Y.T. Liu, Q.Z. Zhu, P. Zhang, Y. Gogotsi, B. Xu, MXene-Bonded Activated Carbon as a Flexible Electrode for High-Performance Supercapacitors, ACS Energy Lett. 3 (7) (2018) 1597–1603, https://doi.org/10.1021/acsenergylett.8b00718.
[17] A.S. Levitt, M. Alhabeb, C.B. Hatter, A. Sarycheva, G. Dion, Y. Gogotsi, Electrospun MXene/carbon nanofibers as supercapacitor electrodes, J. Mater. Chem. A 7 (1) (2019) 269–277.
[18] W. Zheng, P. Zhang, J. Chen, W.B. Tian, Y.M. Zhang, Z.M. Sun, In situ synthesis of CNTs@Ti3C2 hybrid structures by microwave irradiation for high-performance anodes in lithium ion batteries, J. Mater. Chem. A 6 (8) (2018) 3543–3551, https://doi.org/10.1039/c7ta10394h.
[19] M. Hu, R. Cheng, Z. Li, T. Hu, H. Zhang, C. Shi, J. Yang, C. Cui, C. Zhang, H. Wang, B. Fan, X. Wang, Q.-H. Yang, Interlayer engineering of Ti3C2Tx MXenes towards high capacitance supercapacitors, Nanoscale 12 (2) (2020) 763–771.
[20] S. Zheng, C.J. Zhang, F. Zhou, Y. Dong, X. Shi, V. Nicolosi, Z.-S. Wu, X. Bao, Ionic liquid pre-intercalated MXene films for ionogel-based flexible micro-supercapacitors with high volumetric energy density, J. Mater. Chem. A 7 (16) (2019) 9478–9485.
[21] Y. Wen, R. Li, J. Liu, Z. Wei, S. Li, L. Du, K. Zu, Z. Li, Y. Pan, H. Hu, A temperature-dependent phosphorus doping on Ti3C2Tx MXene for enhanced supercapacitance, J. Colloid Interface Sci. 604 (2021) 239–247, https://doi.org/10.1016/j.jcis.2021.06.020.
[22] Z. Zhao, X. Wu, C. Luo, Y. Wang, W. Chen, Rational design of Ti3C2Cl2 MXenes nanodots-interspersed MXene@NiAl-layered double hydroxides for enhanced pseudocapacitor storage, J. Colloid Interface Sci. 609 (2022) 393–402, https://doi.org/10.1016/j.jcis.2021.12.041.
[23] Y. Zhu, K. Rajouâ, S. Le Vot, O. Fontaine, P. Simon, F. Favier, Modifications of MXene layers for supercapacitors, Nano Energy 73 (2020), https://doi.org/10.1016/j.nanoen.2020.104734 104734.
[24] X. Yang, Q. Wang, K. Zhu, K. Ye, G. Wang, D. Cao, J. Yan, 3D Porous Oxidation-Resistant MXene/Graphene Architectures Induced by In Situ Zinc Template toward High-Performance Supercapacitors, Adv. Funct. Mater. 31 (20) (2021) 2101087, https://doi.org/10.1002/adfm.202101087.
[25] S. Chen, Y.F. Xiang, M.K. Banks, C. Peng, W.J. Xu, R.X. Wu, Polyoxometalate-coupled MXene nanohybrid via poly(ionic liquid) linkers and its electrode for enhanced supercapacitive performance, Nanoscale 10 (42) (2018) 20043–20052, https://doi.org/10.1039/c8nr05760e.
[26] H. Niu, Q. Yang, Q. Wang, X. Jing, K. Zhu, K. Ye, G. Wang, D. Cao, J. Yan, Oxygen vacancies-enriched sub-7 nm cross-linked Bi2.88Fe5O12-x nanoparticles anchored MXene for electrochemical energy storage with high volumetric performances, Nano Energy 78 (2020), https://doi.org/10.1016/j.nanoen.2020.105360 105360.
[27] Z. Zou, Q. Wang, J. Yan, K. Zhu, K. Ye, G. Wang, D. Cao, Versatile Interfacial Self-Assembly of Ti3C2Tx MXene Based Composites with Enhanced Kinetics for Superior Lithium and Sodium Storage, ACS Nano 15 (7) (2021) 12140–12150, https://doi.org/10.1021/acsnano.1c03516.
[28] W. Wu, C. Wang, C. Zhao, D. Wei, J. Zhu, Y. Xu, Facile strategy of hollow polyaniline nanotubes supported on Ti3C2-MXene nanosheets for High-performance symmetric supercapacitors, J. Colloid Interface Sci. 580 (2020) 601–613, https://doi.org/10.1016/j.jcis.2020.07.052.
[29] Y. Zhang, P. Chen, Q. Wang, Q. Wang, K. Zhu, K. Ye, G. Wang, D. Cao, J. Yan, Q. Zhang, High-Capacity and Kinetically Accelerated Lithium Storage in MoO3 Enabled by Oxygen Vacancies and Heterostructure, Adv. Energy Mater. 11 (31) (2021) 2101712, https://doi.org/10.1002/aenm.202101712.
[30] H. Li, F. Musharavati, E. Zalenezhad, X. Chen, K.N. Hui, K.S. Hui, Electrodeposited NiCo layered double hydroxides on titanium carbide as a binder-free electrode for supercapacitors, Electrochim. Acta 261 (2018) 178–187, https://doi.org/10.1016/j.electacta.2017.12.139.
[31] H. Li, X. Chen, E. Zalnezhad, K.N. Hui, K.S. Hui, M.J. Ko, 3D hierarchical transition-metal sulfides deposited on MXene as binder-free electrode for high-performance supercapacitors, J. Ind. Eng. Chem. 82 (2020) 309–316, https://doi.org/10.1016/j.jiec.2019.10.028.
[32] H. Chao, H. Qin, M. Zhang, Y. Huang, L. Cao, H. Guo, K. Wang, X. Teng, J. Cheng, Y. Lu, H. Hu, M. Wu, Boosting the Pseudocapacitive and High Mass-Loaded Lithium/Sodium Storage through Bonding Polyoxometalate Nanoparticles on MXene Nanosheets, Adv. Funct. Mater. 31 (16) (2021) 2007636, https://doi.org/10.1002/adfm.202007636.
[33] J.-J. Zhu, R. Benages-Vilau, P. Gomez-Romero, Can polyoxometalates enhance the capacitance and energy density of activated carbon in organic electrolyte supercapacitors?, Electrochim Acta 362 (2020), https://doi.org/10.1016/j.electacta.2020.137007 137007.
[34] Y. Hou, D.F. Chai, B.A. Li, H.J. Pang, H.Y. Ma, X.M. Wang, L.C. Tan, Polyoxometalate-Incorporated Metallacalixarene@Graphene Composite Electrodes for High-Performance Supercapacitors, ACS Appl. Mater. Interfaces 11 (23) (2019) 20845–20853, https://doi.org/10.1021/acsami.9b04649.
[35] M.R. Horn, A. Singh, S. Alomari, S. Goberna-Ferrón, R. Benages-Vilau, N. Chodankar, N. Motta, K. Ostrikov, J. MacLeod, P. Sonar, P. Gomez-Romero, D. Dubal, Polyoxometalates (POMs): from electroactive clusters to energy materials, Energy Environ. Sci. 14 (4) (2021) 1652–1700, https://doi.org/10.1039/d0ee03407j.
[36] S.-C. Huang, C.-C. Lin, C.-W. Hu, Y.-F. Liao, T.-Y. Chen, H.-Y. Chen, Vanadium-based polyoxometalate as electron/ion sponge for lithium-ion storage, J. Power Sources 435 (2019), https://doi.org/10.1016/j.jpowsour.2019.226702 226702.
[37] J. Vaillant, M. Lira-Cantu, K. Cuentas-Gallegos, N. Casañ-Pastor, P. Gómez-Romero, Chemical synthesis of hybrid materials based on PAni and PEDOT with polyoxometalates for electrochemical supercapacitors, Prog. Solid State Chem. 34 (2–4) (2006) 147–159, https://doi.org/10.1016/j.progsolidstchem.2005.11.015.
[38] J. Suarez-Guevara, V. Ruiz, P. Gomez-Romero, Stable graphene-polyoxometalate nanomaterials for application in hybrid supercapacitors, Phys. Chem. Chem. Phys. 16 (38) (2014) 20411–20414, https://doi.org/10.1039/c4cp03321c.
[39] J. Suárez-Guevara, V. Ruiz, P. Gomez-Romero, Hybrid energy storage: high voltage aqueous supercapacitors based on activated carbon–phosphotungstate hybrid materials, J. Mater. Chem. A 2 (4) (2014) 1014–1021, https://doi.org/10.1039/c3ta14455k.
[40] D.P. Dubal, J. Suarez-Guevara, D. Tonti, E. Enciso, P. Gomez-Romero, A high voltage solid state symmetric supercapacitor based on graphene–polyoxometalate hybrid electrodes with a hydroquinone doped hybrid gel-electrolyte, J. Mater. Chem. A 3 (46) (2015) 23483–23492, https://doi.org/10.1039/c5ta05660h.
[41] M. Genovese, K. Lian, Pseudocapacitive behavior of Keggin type polyoxometalate mixtures, Electrochem. Commun. 43 (2014) 60–62, https://doi.org/10.1016/j.elecom.2014.03.014.
[42] V. Ruiz, J. Suarez-Guevara, P. Gomez-Romero, Hybrid electrodes based on polyoxometalate-carbon materials for electrochemical supercapacitors, Electrochem. Commun. 24 (2012) 35–38, https://doi.org/10.1016/j.elecom.2012.08.003.
[43] M. Genovese, K. Lian, Polyoxometalate modified pine cone biochar carbon for supercapacitor electrodes, J. Mater. Chem. A 5 (8) (2017) 3939–3947, https://doi.org/10.1039/c6ta10382k.
[44] S. Kumar, G. Saeed, L. Zhu, K.N. Hui, N.H. Kim, J.H. Lee, 0D to 3D carbon-based networks combined with pseudocapacitive electrode material for high energy density supercapacitor: A review, Chem. Eng. J. 403 (2021), https://doi.org/10.1016/j.cej.2020.126352 126352.
[45] M. Alhabeb, K. Maleski, B. Anasori, P. Lelyukh, L. Clark, S. Sin, Y. Gogotsi, Guidelines for Synthesis and Processing of Two-Dimensional Titanium Carbide (Ti3C2Tx MXene), Chem. Mater. 29 (18) (2017) 7633–7644, https://doi.org/10.1021/acs.chemmater.7b02847.

[46] N. Shpigel, A. Chakraborty, F. Malchik, G. Bergman, A. Nimkar, B. Gavriel, M. Turgeman, C.N. Hong, M.R. Lukatskaya, M.D. Levi, Y. Gogotsi, D.T. Major, D. Aurbach, Can Anions Be Inserted into MXene?, J Am. Chem. Soc. 143 (32) (2021) 12552–12559, https://doi.org/10.1021/jacs.1c03840.
[47] M. Malaki, A. Maleki, R.S. Varma, MXenes and ultrasonication, J. Mater. Chem. A 7 (18) (2019) 10843–10857, https://doi.org/10.1039/c9ta01850f.
[48] S. Zhou, C. Gu, Z. Li, L. Yang, L. He, M. Wang, X. Huang, N. Zhou, Z. Zhang, Ti3C2Tx MXene and polyoxometalate nanohybrid embedded with polypyrrole: Ultra-sensitive platform for the detection of osteopontin, Appl. Surf. Sci. 498 (2019) 143889.
[49] L. Zong, H. Wu, H. Lin, Y. Chen, A polyoxometalate-functionalized two-dimensional titanium carbide composite MXene for effective cancer theranostics, Nano Res. 11 (8) (2018) 4149–4168, https://doi.org/10.1007/s12274-018-2002-3.
[50] L.-Å. Näslund, P.O.Å. Persson, J. Rosen, X-ray Photoelectron Spectroscopy of Ti3AlC2, Ti3C2Tz, and TiC Provides Evidence for the Electrostatic Interaction between Laminated Layers in MAX-Phase Materials, The Journal of Physical Chemistry C 124 (50) (2020) 27732–27742, https://doi.org/10.1021/acs.jpcc.0c07413.
[51] C. Shen, L. Wang, A. Zhou, B. Wang, X. Wang, W. Lian, Q. Hu, G. Qin, X. Liu, Synthesis and Electrochemical Properties of Two-Dimensional RGO/Ti(3)C(2)Tx Nanocomposites, Nanomaterials (Basel) 8 (2) (2018), https://doi.org/10.3390/nano8020080.
[52] J. Wang, J. Polleux, J. Lim, B. Dunn, Pseudocapacitive Contributions to Electrochemical Energy Storage in TiO2 (Anatase) Nanoparticles, The Journal of Physical Chemistry C 111 (40) (2007) 14925–14931, https://doi.org/10.1021/jp074464w.
[53] H. Huang, D. Kundu, R. Yan, E. Tervoort, X. Chen, L. Pan, M. Oschatz, M. Antonietti, M. Niederberger, Fast Na-Ion Intercalation in Zinc Vanadate for High-Performance Na-Ion Hybrid Capacitor, Adv. Energy Mater. 8 (35) (2018) 1802800, https://doi.org/10.1002/aenm.201802800.
[54] L. Hu, R. Gao, A. Zhang, R. Yang, X. Zang, S. Wang, S. Yao, Z. Yang, H. Hao, Y.-M. Yan, Cu2+ intercalation activates bulk redox reactions of MnO2 for enhancing capacitive performance, Nano Energy 74 (2020), https://doi.org/10.1016/j.nanoen.2020.104891 104891.
[55] J. Li, X. Yuan, C. Lin, Y. Yang, L.e. Xu, X. Du, J. Xie, J. Lin, J. Sun, Achieving High Pseudocapacitance of 2D Titanium Carbide (MXene) by Cation Intercalation and Surface Modification, Adv. Energy Mater. 7 (15) (2017) 1602725.